Journal of Materials Science & Technology 84 (2021) 43–48

Contents lists available at ScienceDirect

Journal of Materials Science & Technology

journal homepage: www.jmst.org

A new approach of using Lorentz force to study single-asperity friction inside TEM

Huanhuan Lu [a], Zhangjie Wang [a,*], Di Yun [b], Ju Li [c,*], Zhiwei Shan [a,*]

[a] Center for Advancing Materials Performance from the Nanoscale (CAMP-Nano) and Hysitron Applied Research Center in China (HARCC), State Key Laboratory for Mechanical Behavior of Materials, Xi'an Jiaotong University, Xi'an, 710049, People's Republic of China
[b] School of Nuclear Science and Technology, Xi'an Jiaotong University, Xi'an, 710049, People's Republic of China
[c] Department of Nuclear Science and Engineering and Department of Materials Science and Engineering, Massachusetts Institute of Technology, Cambridge, MA, 02139, USA

ARTICLE INFO

Article history:
Received 11 September 2020
Received in revised form 7 December 2020
Accepted 13 December 2020
Available online 1 February 2021

Keywords:
Single-asperity friction
In situ TEM
Lorentz-force actuation
Maximum friction force
Interfacial failure

ABSTRACT

Taking advantage of the magnetic field inside transmission electron microscope (TEM), a unique Lorentz-force-actuated method for quantitative friction tests was developed *via* a commercial electromechanical holder. With this approach, a submicron-sized silver asperity sliding on a tungsten flat punch was actuated by Lorentz force due to electrical current through the punch, with the normal force imposed by the built-in transducer of the holder. The friction force was determined by tracking the elastic deflection of the fabricated cantilever from *in situ* video. Through correlating the friction behavior with the microstructural evolution near the silver-tungsten interface, we revealed that even when the relative motion commenced with the plastic deformation of the silver asperity, the interface can still sustain the further increasing static friction force. Exactly following the arrival of the maximum static friction force, the sliding occurred at the interface, indicating the transition from static to dynamic friction. This work enriches our understanding of the underlying physics of the dynamic friction process for metallic friction behavior.

1. Introduction

The earliest description for friction phenomena could be traced back to the early Egyptians about four thousand years ago [1], and the first quantitative study of friction force was credited to Leonardo da Vinci [2]. Although explored for such a long time because of the enormous importance of friction in engineering, the fundamental mechanisms of friction behavior are still not well understood. The main reason is that the macroscopic contacting surface consisting of asperities distributed randomly and featured over multiple scales renders it hardly possible to define the interface [3,4], while the fundamental understanding for the friction behavior requires the well-defined interface [5]. The simplified and well-defined interface for fundamental investigations is the single-asperity contact, as the basic unit of the rough contacting surfaces. Thus, to understand the underlying mechanism of the friction behavior at the macroscale, it is necessary to conduct friction investigations of the single-asperity contact at the micro/nanoscale. Friction experiments of single-asperity contacts at the nanoscale are mostly carried out inside the atomic force microscope (AFM) and its modifications [6–8]. AFM has enabled precise control over the loading in the sub-nano Newton regime [9], with the ability to characterize the surface morphology and properties simultaneously [10]. However, the main challenge to interpret AFM experiments is the inability to visualize the contacting surface in real time, which makes it difficult to associate the frictional response with the dynamic phenomena during sliding at the interface [9].

In order to monitor the dynamic evolution of single asperity contacts during sliding, *in situ* transmission electron microscope (TEM) techniques are utilized for the ability to provide the real-time observation of the dynamic process at the sub-nanometer scale [11]. In the last two decades, different types of actuators have been introduced into TEM specimen holders to conduct friction experiments, mainly including piezoelectric [12–15] and electrostatic actuators [16–18]. For example, using the piezoelectric actuator, Merkle and Marks [19] successfully used a tungsten tip to slide on

* Corresponding authors.
E-mail addresses: zhangjiewang@mail.xjtu.edu.cn (Z. Wang), liju@mit.edu (J. Li), zwshan@mail.xjtu.edu.cn (Z. Shan).

https://doi.org/10.1016/j.jmst.2020.12.044
1005-0302/

graphite and directly observed the transfer of graphitic flakes to the tungsten tip, which validated the proposed friction mechanisms to explain the ultralow friction coefficient of graphite. Although being the most widely used actuator integrated into commercial specimen holders, the piezoelectric actuator suffers hysteresis nonlinearity, meaning that the relationship between the output displacement and the input voltage is nonlinear [20]. On the other hand, the frictional experiments in TEM can also be performed by an electrostatic actuator, which was integrated into the micro-electro-mechanical-systems (MEMS) device [16–18]. As an example, Ishida et al. [21] rubbed a pair of nanometer-scale crystalline silicon asperities at ultralow speed and observed the amorphization and plastic deformation at the interface, which is valuable for a better understanding of quasi-static friction. However, electrostatic actuators also suffer from the nonlinear relationship between the output displacement with actuation voltage due to the electrostatic force increasing more rapidly than the spring force [22]. The nonlinear relationship between the input and output signals for both piezoelectric and electrostatic actuators hinders their development towards fast and accurate operations [20,22]. In addition, the actuation or sensing strategies for both piezoelectric and electrostatic actuators are inevitably restricted by the strong magnetic field (~2 T) in TEM [23,24]. Our experiments showed that the displayed value of the commercial electrostatic transducer experienced a load jump from 0 to −140 μN, when TEM was shifted from low magnification mode to high magnification mode with the magnetic field increased from ~20 mT to ~2 T. A figure of the load jump can be found in the Supplementary Figure S1. It indicates that the effects of the magnetic field in TEM on the piezoelectric and electrostatic actuators may not be overlooked.

In this work, taking advantage of the strong magnetic field of TEM, we utilized the Lorentz force induced by the applied electric current *via* the commercial electromechanical holder to perform the quantitative frictional tests. The solid lubricant Ag has been widely used in vacuum environments [25] and is one of the good candidates as next-generation lubricants at micro/nanoscale [16]. Hence, the submicron-sized single silver asperity sliding against the tungsten punch was performed, and the frictional behavior was correlated with the microstructural evolution near the silver-tungsten interface.

2. Materials and methods

2.1. Principles for Lorentz-force-actuated friction test

The strong magnetic field is known to exist in the vicinity of the pole piece in TEM. Consequently, the punch of the commercial electromechanical holder inside TEM would be subject to Lorentz force when the electric current flows through it. The Lorentz force is vertical to both directions of the electric current (along the loading axis of the holder) and the magnetic field. Therefore, actuated by Lorentz force, the punch would deflect vertically to the loading axis of the holder, upgrading the holder from the initial uniaxial loading to the two-dimensional loading, which could be utilized to conduct the friction test. The schematic diagram for the setup of Lorentz-force-actuated friction tests inside TEM is shown in Fig. 1(a), where a cantilever, a punch, and a current source meter are connected in series to form a closed circuit. The cantilever and a part of the punch are exposed to the magnetic field. At first, the normal force F_N was applied to cantilever along the z-axis. Then, when the electric current flowed in the circuit, the punch fixed at the right end would deflect along the x-axis by the Lorentz force F_L and the contacting cantilever started to deflect under the friction force F_f. The Lorentz force on the cantilever is neglected, for its value on the order of nN is three orders of magnitude lower than the Lorentz force on the punch (in μN) (more analysis in Supplementary Materials). F_f can be calculated by the product of the elastic deflection and the stiffness of the cantilever.

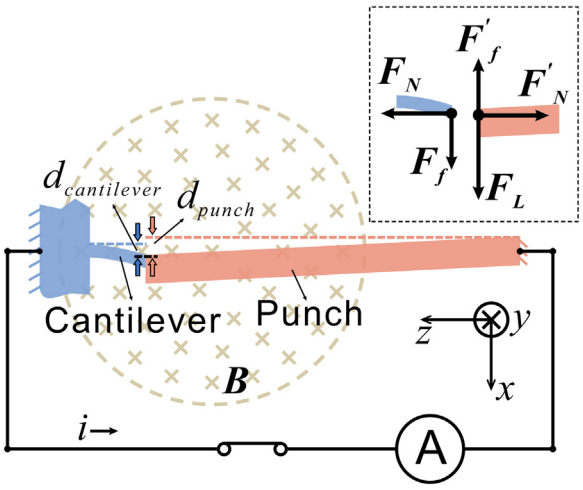

Fig. 1. Schematic diagrams of the Lorentz-force-actuated method for friction experiments inside TEM. The force diagrams in the framed region exhibit that the punch deflects by the Lorentz force and the cantilever deflects under the friction force.

2.2. Sample preparation and test methods

Based on the above experimental design, we have performed friction tests of single-asperity silver-tungsten contacts *via* the *in situ* electromechanical coupling holder (PI95 ECR, Hysitron Inc.) in TEM (JEOL 2100 F), where in the vicinity of the pole piece the magnetic field is about 2 T distributed in a circle with the diameter of ~2.5 mm [23]. The schematic diagram of the silver-tungsten contact is shown in Fig. 2(a). The tungsten punch was electrochemically etched from the 500 μm-diameter polycrystalline rod in the NaOH solution [26] and then milled by a focused ion beam (FIB, FEI Helios NanoLab 600) for a flat rectangular punch with the side edge of several microns. The polycrystalline silver film with about 5.5 μm in thickness was deposited on the silicon wedge [27] by the magnetron sputtering. Then, the submicron-sized silver sample was specially designed and fabricated from the silver film by FIB, with a cuboid cantilever to sustain the elastic deflection combined with the half-cylinder slice for contacting with the tungsten punch, exhibited by the three-dimensional sketch in Fig. 2(a). The loading curve is shown in Fig. 2(b) by the red dots. The normal force was applied along the z-axis to 20 μN at a ramping rate of 5 μN/s and kept for 30 s. A linear electric current was generated by the source meter (Keithley 2602A). With the electric current increasing from 0 (marked by B in Fig. 2(b)) to 8 mA (marked by C in Fig. 2(b)) at the ramping rate of 2 mA/s, the tungsten punch would deflect by Lorentz force from position b to c, and the silver cantilever could deflect from the position outlining by the solid blue line to the dashed blue line under the friction force (caused by the friction force) in Fig. 2(a). The dynamic deflections of the tungsten punch and the silver cantilever and the microstructural evolution at the interface were recorded in real time at 10 frames/s using a Gatan 833 CCD camera. Fig. 2(c) exhibits the TEM frame corresponding to the zero-current point B extracted from the *in situ* video. Through the featured points marked by the solid red and blue triangles, respectively in Fig. 2(c), the deflections of the tungsten punch and the silver cantilever were tracked from the *in situ* video (Supplementary Video S1) using the software (Adobe After Effects CC 15.1.1) and exhibited by solid red and blue dots, respectively with respect to the electric current in Fig. 2(d).

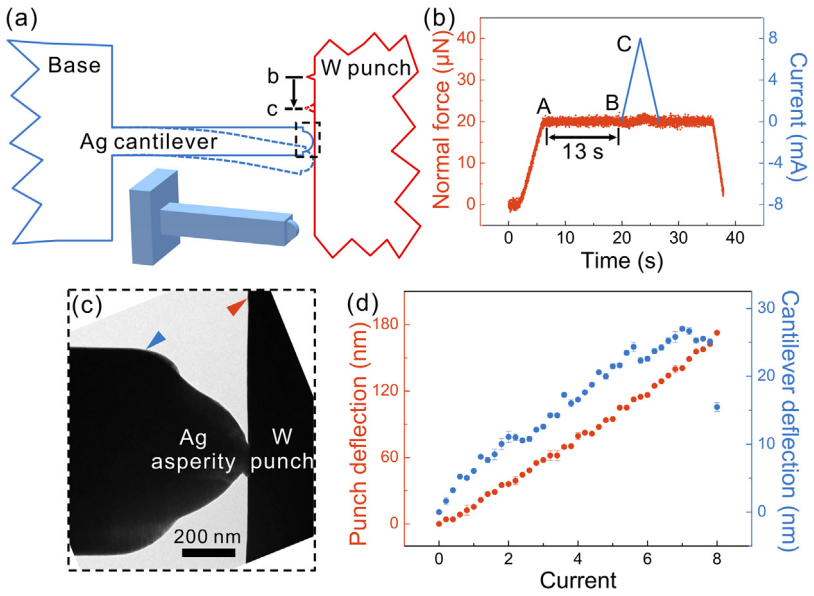

Fig. 2. Silver asperity sliding against tungsten punch under TEM. (a) The schematic diagram shows the deflection of the tungsten punch and the silver cantilever. The inset shows the three-dimensional sketch of the silver cantilever. (b) The electromechanical coupling curve for one cycle of friction test. (c) The frame extracted from the *in situ* video illustrates tracking points of the punch and the cantilever marked by solid red and blue triangles, respectively. (d) The deflection of the tungsten punch and the silver cantilever with respect to the electric current, with the error bars from the standard deviation over six-time tracking measurements.

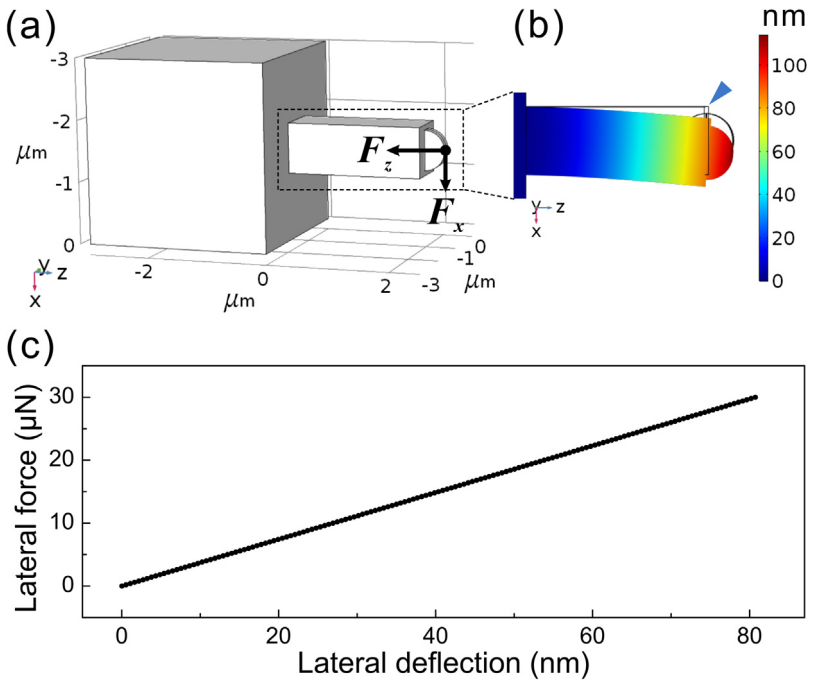

Fig. 3. The finite element analysis for the stiffness of the silver cantilever by the Multiphysics package, COMSOL. (a) The finite element model for the silver cantilever experiencing normal force in the *z*-axis and lateral force along the *x*-axis. (b) The color map for the deflection along the *x*-axis. (c) The lateral force *versus* the deflection along the *x*-axis at the tracking point marked by solid blue triangle in (b), respectively.

2.3. Calculating friction force

The friction force value is the product of the elastic deflection of the cantilever and its stiffness. Specifically, the cantilever deflection is measured from the *in situ* video (blue dots in Fig. 2(d)) and the cantilever stiffness is calculated by finite element analysis. The stiffness of the silver cantilever is determined from the cantilever geometry and the silver properties, including the volumetric mass density, the Poisson's ratio, and Young's modulus. The cantilever geometry is directly measured from SEM (scanning electron microscope) and TEM images. The volumetric mass density and the Poisson's ratio are according to the bulking counterpart value, while the Young's modulus of submicron-sized structures is different from the bulking value due to surface effects [28]. Thus, the cyclic loading-partially unloading tests were carried out to determine the Young's modulus of the silver cantilever (for details, see Figure S2 in the Supplementary data). With the calculated Young's modulus, a finite element model was built by Multiphysics package, COMSOL, as shown in Fig. 3(a) according to the geometry of the silver cantilever, to determine its stiffness, bearing constant

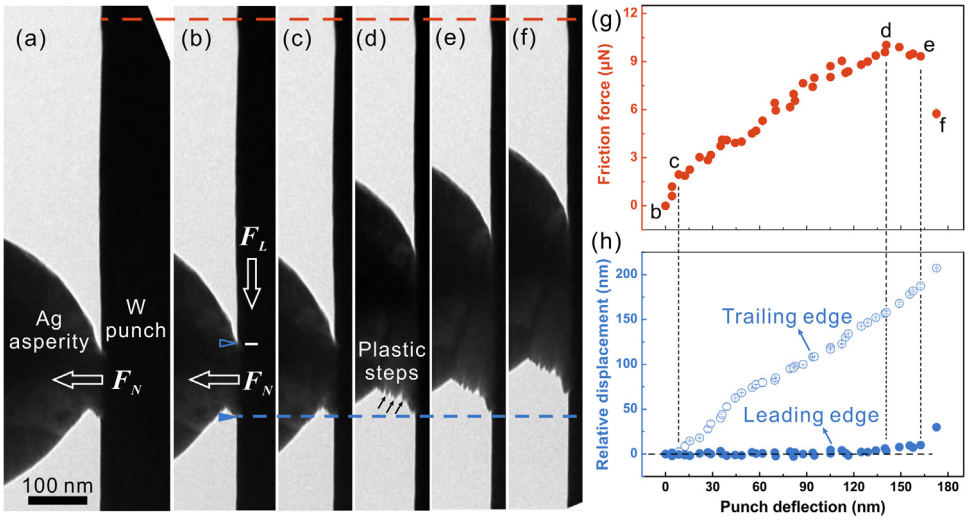

Fig. 4. The transition from static to dynamic friction for the submicron-sized silver-tungsten contact. (a) The frame extracted from the *in situ* video corresponding to the starting point of the constant normal force (20 μN). (b)-(f) Frames corresponding to the b-f points in (g), respectively. (g)-(h) The friction force and relative displacements with respect to the punch deflection, respectively, with error bars calculated by the standard deviation propagation equation.

normal force in the *z*-axis and ramping lateral force in the *x*-axis. The color map for the displacement along the *x*-axis exhibits in Fig. 3(b), the point marked by the solid blue triangle corresponding to the tracking point for the silver cantilever in Fig. 2(c). The lateral force is linearly proportional to the deflection at the tracking point shown in Fig. 3(c), the slope representing the corresponding stiffness. Then, the friction force can be obtained by the product of the elastic deflection extracted directly from the *in situ* video and the corresponding stiffness of the silver cantilever.

3. Results and discussion

3.1. Microstructural evolution near the interface during friction process

Prior to applying the electric current, the normal force was kept at 20 μN for about 13 s. During this duration, no obvious plastic deformation occurred to the silver asperity by comparing frames in Fig. 4(a) to (b). Once applying the electric current, the silver asperity was observed to deflect with the tungsten punch from Fig. 4(b).

For accurately capturing the relative motion at the interface, all the frames were aligned by the featured point of the tungsten punch, exhibited by the dashed red line across Fig. 4(a)-(f). The leading and trailing edges of the tungsten-silver contact were determined and marked by the solid and empty blue triangles in Fig. 4(b), as the tungsten punch moved downward along F_L direction. The relative displacement between the leading edge and the tungsten punch was calculated by the distance between the solid blue triangle and the aligned dashed red line subtracting its initial value at Fig. 4(b). And the relative displacement of the trailing edge was obtained similarly. The relative displacements of leading and trailing edges *versus* punch deflection were exhibited in Fig. 4(h), marked by solid and empty blue circles, respectively. To correlate the friction behavior with the microstructural evolution near the interface, the friction force *versus* the punch deflection was shown in Fig. 4(g), and frames extracted from the *in situ* video were shown in Fig. 4(b) to (f), corresponding to the points b–f in Fig. 4(g), respectively.

Three stages could be distinguished during the friction process. First, from point b to c, the friction force increased linearly with the punch deflection, and no obvious plastic deformation occurred, as illustrated in Fig. 4(c). During this stage, the relative displacements of the leading and trailing edges both were almost zero. Second, from point c to d, the friction force further increased, but deviating from the linearity and the silver asperity experienced obvious plastic deformation, as illustrated with plastic steps marked by dark arrows near the leading edge in Fig. 4(d). Simultaneously, the relative displacement of the leading edge further kept almost zero, while that of the trailing edge started to increase due to the rise of the contact length induced by the plastic deformation. Thus, the relative motion incepting at the trailing edge was ascribed to the plastic deformation of the silver asperity. Third, from point d to f, the friction force began to decrease slightly and quickly experienced a sudden drop after point e. Correspondingly, the relative displacement of the leading edge increased slightly after point d and suddenly rose after point e, indicating the occurrence of sliding at the interface. Hence, the friction force arrived at its maximum value exactly followed by the interface sliding.

3.2. The transition from static to dynamic friction

The study of the transition from static to dynamic friction is central to frictional fields ranging from single nanometric contacts for revealing the atomistic origin of friction [29,30] to the natural geological faults for predicting earthquakes [31] regarded as a sudden slippage along the fault interface [32]. Conventionally, the onset of dynamic friction is known to commence with the relative motion at the interface, corresponding to the arrival of the maximum friction force [33,34]. However, recent publications reported that at the macroscale the relative motion occurred before the maximum friction force arrived [35–37], which is explained by the "partial sliding" conjecture meaning that part of asperities slides locally at the microscale before the full sliding at the macroscale [38]. This conjecture is difficult to be verified, restricted by the resolution of the optical methods in macroscopic experiments. Here, we try to explain this doubt from the single-asperity friction at the microscale.

Our experimental results demonstrated that for the submicron-sized and deformable single-asperity contact, both the plastic deformation of the asperity and the interface sliding can contribute to the relative motion. The friction force increased further due to the working hardening of silver asperity after the occurrence of plastic deformation, while arrived at its maximum value exactly followed by the interface sliding. Thus, the interface sliding indi-

cates the interfacial failure, when no more external lateral force can be sustained. Presumably, for deformable metallic contacts at the macroscale consisting of lots of microscopic asperities, with the external lateral force increasing gradually, more and more asperities experience plastic deformation resulting in the onset of relative motion and the further increase of the friction force. Then, more and more asperities experience interface sliding locally, and the friction force would arrive at its maximum value until the number of sliding asperities reaches a critical value, where the macroscopic sliding would occur. Hence, through concrete experimental evidence distinguishing the relative motion stemming from the plastic deformation and the interface sliding and their contribution to the friction force, we can understand the macroscopic friction phenomenon that the friction force increases further after the occurrence of the relative motion.

3.3. The advange of the Lorentz-force-actuated approach in system control

Conventional friction measurements are actuated by piezoelectric or electrostatic actuators. Our setup distinguishes itself from the piezoelectric and electrostatic actuators by the linear relationship between the input electric current and the output Lorentz force. The piezoelectric actuator suffers from the hysteresis nonlinearity (the nonlinear phenomenon between the applied voltage and the output displacement) stemming from the inherent property of piezoelectric materials [39,40]. As for the electrostatic actuator, the electrostatic force is inversely related to the square of the gap between the parallel plates and balanced by the spring force (proportional to the gap) from the flexible beam suspending the movable plate [41]. Consequently, the relationship between the input voltage and the output displacement is nonlinear. For both piezoelectric and electrostatic actuators, the nonlinearity between the input and output signals could lead to the instability of the system [42,43], and they need extra feedback control design to improve the stability of the overall system [44]. Our new approach, the Lorentz force serving as actuating force is linearly proportional to the input electric current. According to the force diagrams in Fig. 1, for the punch at the contact surface along x-direction, the Lorentz force

$$F_L = aI = F_f^{'} + k_{punch} \cdot d_{punch} \tag{1}$$

where a is a constant relevant to the magnetic field strength and the punch length, I is the flowing electric current, and k_{punch} and d_{punch} are the stiffness and the deflection of the punch, respectively.

For the cantilever at the contact surface along x-direction,

$$F_f = k_{cantilever} \cdot d_{cantilever} \tag{2}$$

where $k_{cantilever}$ and $d_{cantilever}$ are the stiffness and the deflection of the cantilever, respectively.

At the interface,

$$F_f^{'} = F_f \tag{3}$$

Substituting Eqs. (2) and (3) into (1), the following equation was obtained.

$$aI = k_{cantilever} \cdot d_{cantilever} + k_{punch} \cdot d_{punch} \tag{4}$$

As illustrated in Eq. (4), theoretically, for any value of I, effective values of $d_{cantilever}$ and d_{punch} can be obtained. Thus, our Lorentz-force-actuated system can be stable with open-loop control, exceeding the piezoelectric and electrostatic actuation in micro/nanoscale with the bulky close-loop control system.

3.4. The resolution and the accuracy of the experimental measurements

The image resolution of the *in situ* video is 1.03 nm/pixel, depending on the magnification and recording settings of the CCD camera. The punch deflection was tracked by the software from the video at the feature point on the punch, providing the tracking accuracy in sub-pixel [45]. We made the tracking measurements for six times, the standard deviation of the punch deflection was 0.6 nm under the electric current of 8 mA, which mainly resulted from the random error for the selection of feature points using naked eyes and the tracking accuracy of the software dependent on the contours, the definition, and the contrast of the tracking feature [45].

4. Conclusions

In this work, taking advantage of the strong magnetic field in TEM, we developed a new approach to conduct the quantitative frictional experiments of single-asperity contacts. Our experiments demonstrated that for submicron-sized and deformable single-asperity contacts, the relative motion was initiated with the plastic deformation of the silver asperity before the friction force arrived at its maximum values exactly followed by the interface sliding. This work helps us to understand the dynamic process of the transition from static to dynamic friction for metallic contacts at the macroscale from the view of submicron-sized single-asperity contact.

Declaration of Competing Interest

The authors declare that they have no known competing financial interests or personal relationships that could have appeared to influence the work reported in this paper.

Acknowledgments

The authors gratefully acknowledge the support by the National Key Research and Development Program of China (2017YFB0702001), National Natural Science Foundation of China (51971167). We also appreciate the support from the International Joint Laboratory for Micro/Nano Manufacturing and Measurement Technologies and the Collaborative Innovation Center of High-End Manufacturing Equipment and 111 Project 2.0 (BP2018008). J. Li acknowledges support by NSF CBET-2034902.

Appendix A. Supplementary data

Supplementary material related to this article can be found, in the online version, at doi:https://doi.org/10.1016/j.jmst.2020.12.044.

References

[1] I. Svetlizky, E. Bayart, J. Fineberg, Annu. Rev. Condens. Matter Phys. 10 (2019) 253–273.
[2] I.M. Hutchings, Wear 360-361 (2016) 51–66.
[3] H. Ghaednia, X. Wang, S. Saha, Y. Xu, A. Sharma, R.L. Jackson,Appl. Mech. Rev. 69 (2017), 060804.
[4] R.W. Carpick, Science 359 (2018), 38-38.
[5] I. Szlufarska, M. Chandross, R.W. Carpick,J. Phys. D Appl. Phys. 41 (2008), 123001.
[6] C.M. Mate, G.M. Mcclelland, R. Erlandsson, S. Chiang, Phys. Rev. Lett. 59 (1987) 1942–1945.
[7] R.W. Carpick, N. Agrait, D.F. Ogletree, M. Salmeron, J. Vac. Sci. Technol. B 14 (1996) 1289–1295.
[8] H. Bhaskaran, B. Gotsmann, A. Sebastian, U. Drechsler, M.A. Lantz, M. Despont, P. Jaroenapibal, R.W. Carpick, Y. Chen, K. Sridharan, Nat. Nanotechnol. 5 (2010) 181–185.

[9] R.W. Carpick, Proc. STLE/ASME Int. Jt. Tribol. Conf. 43369 (2008) 95–97.
[10] T.D.B. Jacobs, C. Greiner, K.J. Wahl, R.W. Carpick, MRS Bull. 44 (2019) 478–486.
[11] Y. Liao, L. Marks, Int. Mater. Rev. 62 (2017) 99–115.
[12] T. Kizuka, Phys. Rev. B 57 (1998) 11158–11163.
[13] K. Svensson, Y. Jompol, H. Olin, E. Olsson, Rev. Sci. Instrum. 74 (2003) 4945–4947.
[14] R. Ribeiro, Z. Shan, A.M. Minor, H. Liang, Wear 263 (2007) 1556–1559.
[15] K. Anantheshwara, M.S. Bobji, Tribol. Int. 43 (2010) 1099–1103.
[16] T. Sato, T. Ishida, L. Jalabert, H. Fujita, Tribol. Online 6 (2011) 226–229.
[17] S. Takaaki, I. Tadashi, J. Laurent, F. Hiroyuki,Nanotechnology 23 (2012), 505701.
[18] T. Sato, L. Jalabert, H. Fujita, Microelectron. Eng. 112 (2013) 269–272.
[19] A.P. Merkle, L.D. Marks,Appl. Phys. Lett. 90 (2007), 064101.
[20] S.O.R. Moheimani,Rev. Sci. Instrum. 79 (2008), 071101.
[21] T. Ishida, T. Sato, T. Ishikawa, M. Oguma, N. Itamura, K. Goda, N. Sasaki, H. Fujita, Nano Lett. 15 (2015) 1476–1480.
[22] Y. Sun, D. Piyabongkarn, A. Sezen, B. Nelson, R. Rajamani, Sens. Actuator A: Phys. 102 (2002) 49–60.
[23] D.B. Williams, C.B. Carter, Transmission Electron Microscopy: A Textbook for Materials Science, Springer, 2009.
[24] O.L. Warren, S.S. Asif, E. Cyrankowski, K. Kounev, Actuatable capacitive transducer for quantitative nanoindentation combined with transmission electron microscopy, US Patent, No. 7798011 B2, 2010.
[25] M. Goto, F. Honda, M. Uemura, Wear 252 (2002) 777–786.
[26] P. Zhang, P. Chai, X. Zhao, Z. Shan, Microsc. Microanal. 22 (2016) 174–175.
[27] Y. Wang, W. Zhang, L. Wang, Z. Zhuang, E. Ma, J. Li, Z. Shan, NPG Asia Mater. 8 (2016) e291–297.
[28] S.G. Nilsson, X. Borrise, L. Montelius, Appl. Phys. Lett. 85 (2004) 3555–3557.
[29] S. Li, Q. Li, R.W. Carpick, P. Gumbsch, X.Z. Liu, X. Ding, J. Sun, J. Li, Nature 539 (2016) 541–545.
[30] K. Tian, N.N. Gosvami, D.L. Goldsby, Y. Liu, I. Szlufarska, R.W. Carpick,Phys. Rev. Lett. 118 (2017), 076103.
[31] M. Ohnaka, The Physics of Rock Failure and Earthquakes, Cambridge University Press, 2013.
[32] C.H. Scholz, Nature 391 (1998) 37.
[33] B. Bhushan, Handbook of Micro/Nanotribology, second edition, CRC Press, 1999.
[34] B. Jeremic, D. Vukelic, P.M. Todorovic, I. Macuzic, M. Pantic, D. Dzunic, B. Tadic, J. Frict. Wear 34 (2013) 114–119.
[35] I. Etsion, O. Levinson, G. Halperin, M. Varenberg, J. Tribol. 127 (2005) 47–50.
[36] A. Ovcharenko, G. Halperin, I. Etsion, M. Varenberg, Tribol. Lett. 23 (2006) 55–63.
[37] A. Pougis, S. Philippon, R. Massion, L. Faure, J.J. Fundenberger, L.S. Toth, Tribol. Int. 67 (2013) 27–35.
[38] A. Wu, X. Shi, A.A. Polycarpou,J. Appl. Mech. 79 (2012), 051001.
[39] S.-B. Choi, Y.-M. Han, Piezoelectric Actuators: Control Applications of Smart Materials, CRC Press, 2010.
[40] S.J. Rupitsch, Piezoelectric Sensors and Actuators, Springer, 2019.
[41] W.-M. Zhang, G. Meng, D. Chen, Sensors 7 (2007) 760–796.
[42] G. Gu, L. Zhu, C. Su, H. Ding, S. Fatikow, IEEE Trans. Autom. Sci. Eng. 13 (2016) 313–332.
[43] W.-M. Zhang, H. Yan, Z.-K. Peng, G. Meng, Sens. Actuator A: Phys. 214 (2014) 187–218.
[44] M. Rakotondrabe, IEEE Trans. Autom. Sci. Eng. 8 (2011) 428–431.
[45] M. Christiansen, Adobe After Effects CS5 Visual Effects and Compositing Studio Techniques, Pearson Education, 2010.

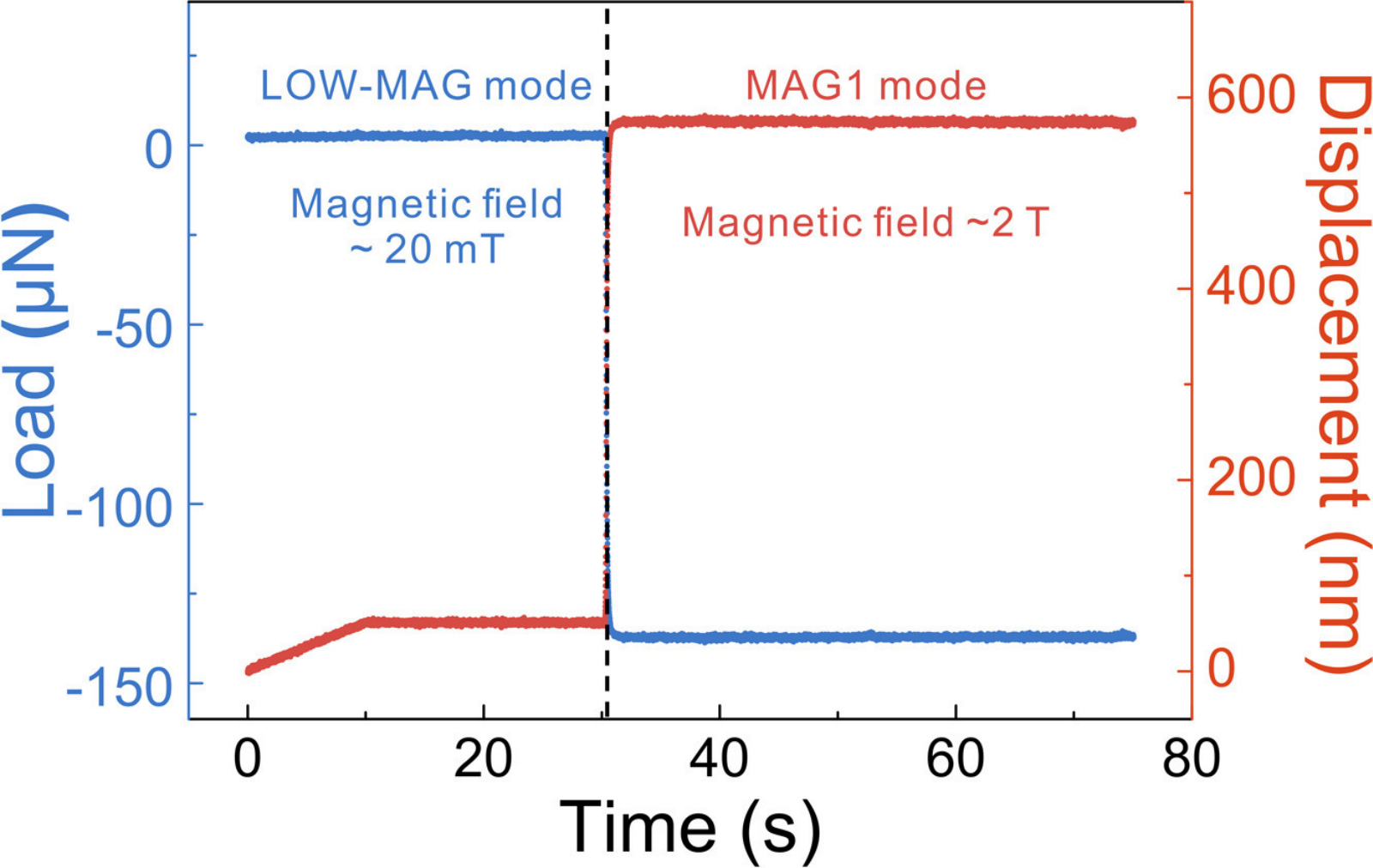
LOW-MAG mode
MAG1 mode
Magnetic field
~ 20 mT
Magnetic field ~2 T
Load (μN)
Displacement (nm)
Time (s)
0
-50
-100
-150
600
400
200
0
0
20
40
60
80

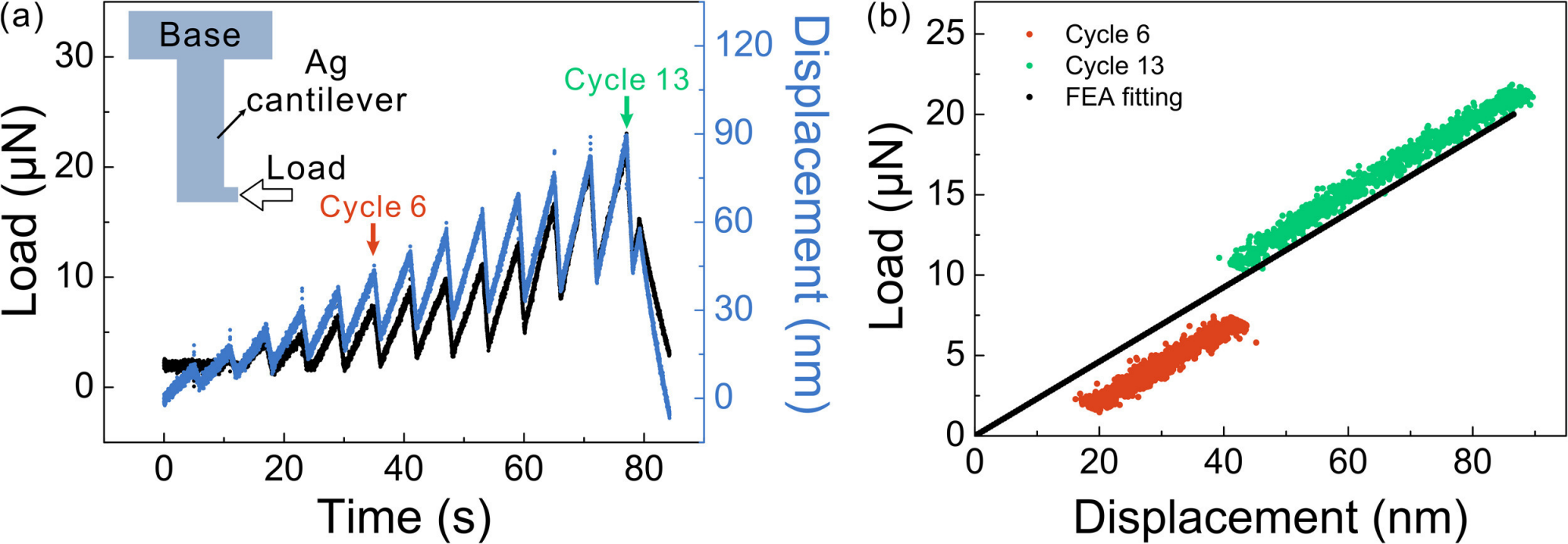
(a)
Base
Ag
cantilever
Load
Cycle 6
Cycle 13
Load (μN)
Displacement (nm)
Time (s)
0
20
40
60
80
0
10
20
30
0
30
60
90
120
(b)
Cycle 6
Cycle 13
FEA fitting
Load (μN)
Displacement (nm)
0
5
10
15
20
25
0
20
40
60
80